Journal of Physics: Conference Series **606** (2015) 012011 doi:10.1088/1742-6596/606/1/012011

Germanium detectors with sub-keV sensitivities for neutrino and dark matter physics

Arun Kumar Soma and Henry Tsz-King Wong
(On behalf of the TEXONO Collaboration)
Institute of Physics, Academia Sinica, Taipei 11529, Taiwan
E-mail: arunsoma@phys.sinica.edu.tw, htwong@phys.sinica.edu.tw

Abstract. A detector of $\mathcal{O}$(1 kg) modular mass with $\mathcal{O}$(100 eV) threshold at $\mathcal{O}$(1 kg^{-1}keV^{-1}day^{-1}) background level finds tremendous application in the field of neutrino and dark matter physics. This novel detector demands overcoming several challenges at both hardware and software levels. The collaboration is exploring Germanium detection technology and highlights of the R & D program are presented. The salient features of various detector configuration and the applied analysis methodologies are discussed. In particular the differentiation of surface and bulk events by pulse shape analysis in point contact Germanium detector is described. These advances pave the way for new detector technique to be fully exploited.

1. Physics motivations

Germanium (Ge) detectors offer potential for realizing $\mathcal{O}$(1 kg) modular mass, $\mathcal{O}$(100 eV) threshold and $\mathcal{O}$(1 kg^{-1}keV^{-1}day^{-1}) background level experiments. When these benchmark specifications are fulfilled, several topics discussed in subsequent sub-sections can be experimentally pursued.

1.1. Neutrino electromagnetic properties

The studies on possible neutrino electromagnetic interactions [1] can probe physics beyond the Standard Model. Neutrino magnetic moments (μ_ν) is an intrinsic neutrino property that describes possible neutrino-photon couplings via its spin [2, 3]. The helicity is flipped in μ_ν induced interactions. Observations of μ_ν at levels relevant to present or future generations of experiments will strongly favor the neutrinos are Majorana particles [4]. As shown in Figure 1a, the μ_ν contributions are enhanced as T decreases, with modifications of the atomic binding energy effects [5]. Where, T denotes the measurable energy in the detector (in this case it originates from the recoil energy of electron).

In a similar spirit, studies of neutrino "milli-charge" (Q_ν) probe possible helicity-conserving QED-like interactions. Finiteness of Q_ν would imply neutrinos are Dirac particles. It was recently recognized that there is enhancement in cross-sections due to atomic effects [6], as depicted in Figure 1a. The known ratios of the peaks and discrete binding energies provide smoking gun signatures for positive observations.

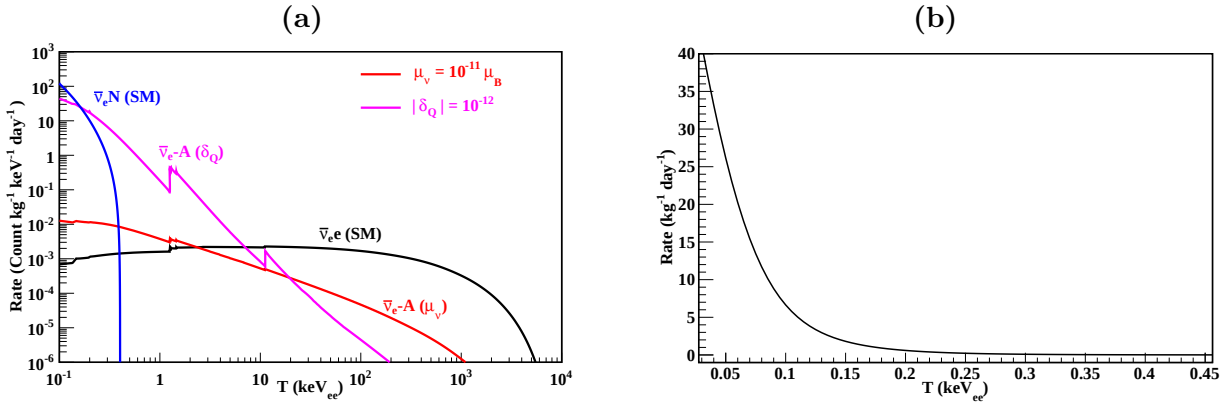

Figure 1. (a) The observable spectra due to neutrino interactions on Ge target with reactor $\bar{\nu}_e$ at $\phi(\bar{\nu}_e)$=10^{13} cm^{-2}s^{-1}. The neutrino magnetic moment (MM) contributions to $\bar{\nu}_e$-e at $\mu_\nu = 10^{-10}\ \mu_B$, as well as the Standard Model (SM) $\bar{\nu}_e$-e and coherent scattering $\bar{\nu}_e$-N are shown. (b) Expected integral $\bar{\nu}_e$-N coherent scattering rates due to SM contributions as a function of detector threshold, assuming realistic detector resolution.

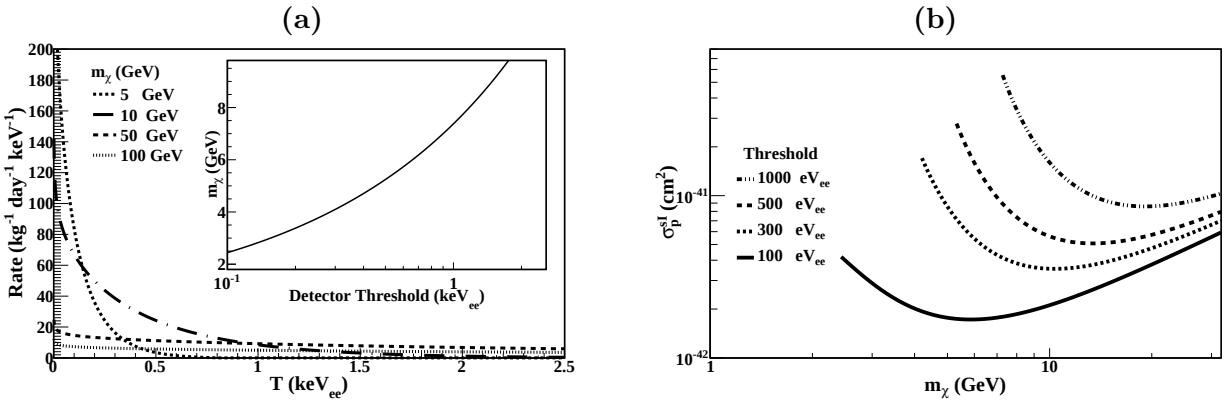

Figure 2. (a) Measurable recoil spectra for WIMP-Ge interactions at a cross-section of 10^{-40} cm^2, at several values of m$_\chi$. The lower bounds of the m$_\chi$ which can be probed with 1 kg-yr of data at background level of 1 kg^{-1}keV^{-1}day^{-1} as a function of physics threshold is shown in the inset. Quenching effects of nuclear recoils are taken into account. (b) Sensitivity reach of the same configuration at different detector threshold, showing the relative improvement in cross-section as a function of m$_\chi$.

1.2. Neutrino nucleus coherent scattering

Neutrino coherent scattering with the nucleus ($\nu + N \rightarrow \nu + N$, νN) [7] is a fundamental neutrino interaction which has never been observed. Measurement of νN coherent scattering would provide a sensitive test to the Standard Model. The coherent interaction plays an important role in astrophysical processes. They may provide new approaches towards the detection of supernova neutrinos and offer a promising avenue towards a compact and relatively transportable neutrino detector for real-time monitoring of nuclear reactors.

The maximum nuclear recoil energy for Ge target (A=72.6) due to reactor $\bar{\nu}_e$ is about 2 keV. The quenching factor is about 20% for Ge in the <10 keV region. Accordingly, the maximum measurable energy is about 400-500 eV [12]. The typical differential spectrum and the integral

event rate as a function of measurement threshold are given in Figures 1a&b, respectively. At the benchmark sensitivities, the expected rate is $\mathcal{O}(10\ \ \mathrm{kg^{-1}day^{-1}})$ with signal to background ratio >50 at threshold of 100 $\mathrm{eV_{ee}}$. Low detector threshold is therefore crucial in such experiments.

1.3. Dark matter searches

The WIMP interaction with matter [8] ($\chi + N \rightarrow \chi + N$) is predominantly via the same coherent scattering mechanism like that of neutrinos. The major difference is that cosmology requires the WIMPs to be massive and its motion is non-relativistic to be consistent with observational data on structure formation [8]. In addition, there may be both spin-independent and spin-dependent interactions between WIMP and matter. The nuclear recoil spectra at 10^{-40} $\mathrm{cm^2}$ for several WIMP mass ($\mathrm{m_\chi}$) for Ge are displayed in Figure 2a.

Therefore, the advantages of having a low threshold detector are as follows:

(i) WIMPs with lower masses would become detectable when nuclear recoils at lower energy can be measured, thereby opening a new window of observation. The sensitivity reach of $\mathrm{m_\chi}$ with 1 kg-yr of data strength as a function of threshold at a background of 1 $\mathrm{kg^{-1}keV^{-1}day^{-1}}$ is illustrated in the inset of Figure 2a.

(ii) The low threshold allows a larger range of WIMPs to contribute in an observable interaction and hence results in better sensitivities for all values of m_χ, as illustrated Figure 2b.

2. Experimental configuration

The Ge detection technology is being explored by TEXONO [11] and CDEX [14] experiments at Kuo-Sheng Reactor Neutrino Laboratory (KSNL, 28 meters from a 3 GW thermal power reactor core, 30 meter-water-equivalent overburden) and China Jinping Underground Laboratory (CJPL, >2400 m of rock overburden with drive-in access), respectively. The reasons for exploring the Ge detection technology are as follows:

(i) Ge is a semiconducting material with an band-gap of ∼0.66 eV at 300 K and requires ∼2.96 eV for an electron-hole pair at 77 K [9]. Therefore, sub-keV threshold detectors can be fabricated.

(ii) Ge detection technology is well matured. Therefore, desired radio-purity and detectors with larger modular mass can be constructed.

2.1. Active and passive shielding

The "baseline design" is shown in the Figure 3. Ge detectors are enclosed by an NaI(Tl) anti-Compton (AC) detector and copper passive shielding inside a plastic bag purged by nitrogen gas evaporated from liquid nitrogen dewar. The set-up is further shielded by copper, boron-loaded polyethylene, steel and lead. At the surface laboratory (KSNL), an additional shielding in the form of cosmic-ray (CR) veto panels comprising of plastic scintillators that are read out by photomultipliers is deployed. The AC and CR detectors are crucial and serve as vetos to reject background and as tags to identify samples for efficiency measurements. The details of signal processing and data analysis can be referred to [11, 14, 15].

2.2. Sub-keV threshold Ge detectors

TEXONO collaboration has studied operational characteristics and performance of various commercially constructed Ge detectors. The four kinds of detector configurations used[12] are listed below with their corresponding sensor schematics depicted in Figure 4.

(i) 1 kg coaxial p-type high purity Ge detector used as target detector in Ref. [3],

(ii) 4×5 g n-type Ge detector array (ULEGe) used as target detector in Refs. [10, 13],

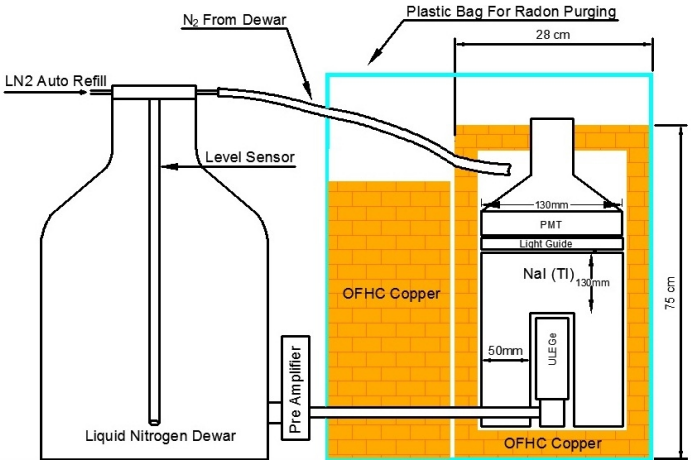

Figure 3. Schematic diagram of experimental set-up that includes Ge and NaI(Tl) scintillator along with 50-tons of passive shielding structure.

(iii) 900 g p-type point-contact Ge detector (pPCGe) used as target detector in Refs. [11, 14] and

(iv) 500 g n-type point-contact Ge detector (nPCGe) used for calibration in Refs. [11, 15].

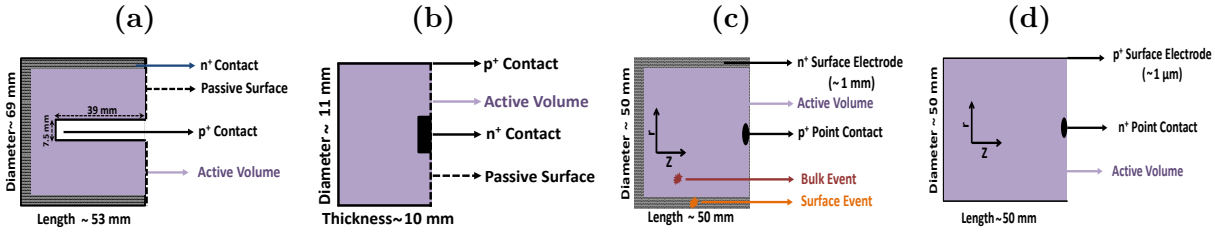

Figure 4. Schematic crystal configurations of the Ge detectors: (a) coaxial HPGe at 1 kg mass (b) ULEGe at 5 g modular mass (c) pPCGe at 900 g mass and (d) nPCGe at 500 g mass.

The HPGe and ULEGe are conventional technologies. The concept of point-contact Ge detectors was proposed and the first nPCGe at 800 g mass was constructed in the 1980's [16], followed by recent realization of pPCGe [17]. The ULEGe, pPCGe and nPCGe are of sub-keV sensitivities and with typically ∼pF capacitance.

A summary of detectors performance is given in Table 1. PCGe detectors are the focuses of subsequent discussions and are adopted as "Reference" detector to illustrate characterization processes and evolution of background spectra with software selection procedures.

The crystal of pPCGE is made of p-type Ge. The outer surface electrode is at positive high voltage towards which the electrons are drifted. The central point contact electrode is at zero-potential. The outer surface electrode is fabricated by lithium diffusion and its thickness is ∼1 mm. The electron-hole pairs produced by radiations at surface (S) layer are subjected to a weaker drift field than those at the bulk (B) region of crystal. A portion of the pairs will recombine while the residual will induce signals which are weaker and slower than those originated in B. Therefore, S-events have partial charge collection and slower rise-time [15].

The pre-amplifiers are coupled to point and surface contact from which electrical signals are extracted. These signals are then processed by shaping and timing amplifiers before feeding to

Table 1. Summary table on the performance of various Ge detectors.

Items	HPGe	ULEGe	pPCGe	nPCGe
Modular Mass (g)	1000	5	900	500
RESET Amplitude (V)	N/A †	8.0	9.8	6.8
RESET Time Interval (ms)	N/A †	700	800	170
Pedestal Noise				
Amplitude RMS σ_A (eV)	812	15	56	49
Charge(Energy) RMS σ_Q (eV)	840	38	79	52
Pulser Width				
FWHM (eV)	1566	80	141	133
RMS (eV)	665	34	60	57
Gamma Line Width	Ga-K X-Ray	^{55}Fe	Ga-K X-Ray	Ga-K X-Ray
RMS (eV)	910	78	157	134
Selected Trigger Level Δ (σ_A)	3.58	4.3	3.64	3.73
50% Trigger Efficiency (eV)	3500	80	230	200
Trigger Rate (Hz)	60	5	42	36
50% Selection Efficiency (eV)	4200	220	400	300
Noise Edge "NoEd" (eV)	5000	320	550	350

† HPGE uses Resistance feedback preamplifier and so not applicable (N/A).

60 MHz and 200 MHz digitizes, respectively. The process of noise and background suppression are presented in the next section.

The thickness of S layer was measured to be (1.16±0.09)mm by comparing intensity ratios of simulated and observed γ-peaks from ^{133}Ba source [18]. The corresponding fiducial mass for B-region is 840 g.

2.3. Physics event selection

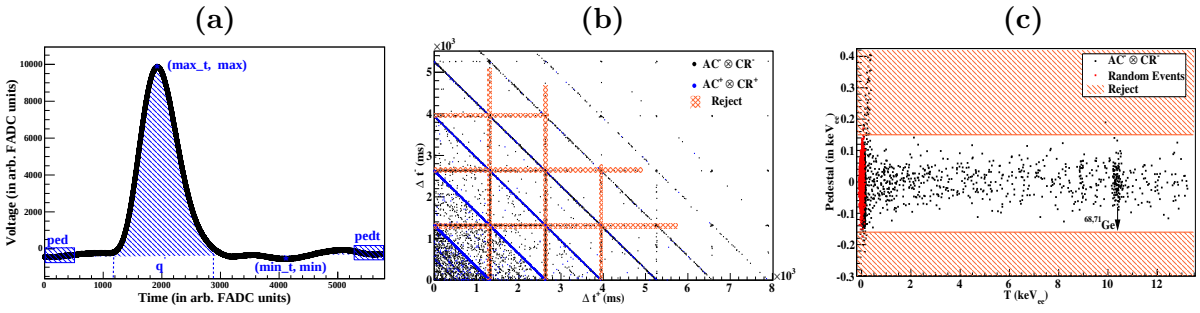

Figure 5. (a) Shaping amplifier (Canberra 2026) output with definitions of some of the analysis parameters; (b) Events timing with respect to reset signal, where Δt^+ and Δt^- are correspondingly the next and previous reset signal; (c) events selection based on fluctuation of pedestal.

A typical shaping amplifier (SA) output pulse is shown in Figure 5a. The waveform is characterized by several parameters and some of them are shown in Figure 5a. The noise events are then eliminated by exploring correlations between the stored waveform parameters. For

example, events timing correlated with pre-amplifier reset signal and distribution of pedestal are shown in Figure 5b and 5c, respectively. The cumulative efficiency of all such cuts (PN: Physics and Noise) is shown in Figure 8c.

The energy calibration was performed by using $X - rays$ from ^{68}Ge (10.37 keV), ^{68}Zn (8.98 keV), and $^{68}Ge + {}^{65}Zn$ (1.29 keV) with random trigger events providing zero-energy definition [12].

The nuclear recoil χN and νN events are uncorrelated with other detector components and are uniformly distributed in pPCGe volume. If superscript $-/(+)$ denotes anti-coincidence (coincidence) of cosmic ray and anti-Compton veto systems with pPCGe signals, then desired signal events are designated by $AC^{-}\otimes CR^{-}$. The $AC^{+}\otimes CR^{-}$ and $AC^{-}\otimes CR^{+}$ select ambient gamma and cosmic ray induced high energy neutron events, respectively.

3. Differentiation of bulk and surface events

The typical pulse shape of fast-timing amplifier (TA) are shown in Figure 6. The B&S events at 2 keV_{ee} and 700 eV_{ee} are respectively depicted in Figure 6a&b.

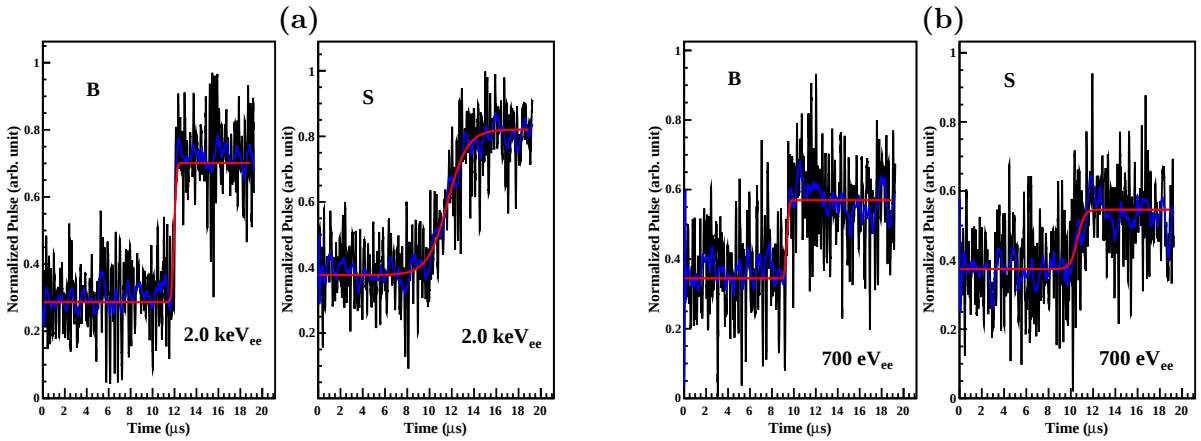

Figure 6. Typical S/B events at (a) 2 $keVee$ and (b) 700 $eVee$ energy with raw pulses shown in black. The smoothed (blue) pulses, together with the best-fit functions(red) are also superimposed.

The rise-time of TA pulse were evaluated by using the hyperbolic tangent function:

$$\frac{\mathrm{A_0}}{2}\tanh(\frac{t-\mathrm{t_0}}{\tau}) + \mathrm{P_0} \quad (1)$$

where, $\mathrm{A_0}$, $\mathrm{P_0}$ and $\mathrm{t_0}$ are amplitude, pedestal offset and timing offset, respectively.

$\mathrm{P_0}$ and $\mathrm{A_0}$ are evaluated from the TA-pulses through the difference of asymptotic levels, respectively. The time difference as a function of energy between the TA-edge and the DAQ-trigger instant defined by SA signals is predetermined, and provides constraints on $\mathrm{t_0}$.

TA amplitude becomes comparable to noise fluctuations at threshold. Therefore, TA pulses were first smoothed by Savitzky-Golay filters [19] with (τ,$\mathrm{t_0}$) as free parameters. The obtained fitting parameters were then employed as initial values to fit raw TA pulses and final fitting parameters were obtained. The smoothed and final fit are shown by blue and red lines in Figure 6.

The scatter plot of τ versus T for $AC^{-}\otimes CR^{-}$ events is shown in Figure7a&b for pPCGe and nPCGe, respectively. For pPCGe, events with τ less(greater) than a selected cut-value τ_0

(=1.23 μs) are categorized as B(S). In contrast, nPCGe does not exhibit anomalous surface events, as illustrated in Figure 7b where the S-band is totally absent.

The width of measured B and S bands at $T > 1.5$ keV_{ee} is much less than separation of bands from τ_0. Therefore, measured τ provides valid information on locations of events and efficiently differentiate S and B events. This behavior also manifests as distinct two band structures in Figure 7a, with a small fraction (about 8% within 3−6 keV_{ee} of $AC^- \otimes CR^-$) of events in intermediate transition zone. By studying the corresponding fractions of events with ^{241}Am (<1%) and ^{137}Cs (7.5%) γ-sources, a thickness of 0.16 mm for this zone was derived. The choice of τ_0 is equivalent to defining the spatial borderline between B/S within this transition thickness. This gives rise to a systematic uncertainty in evaluation of pPCGe fiducial mass. It translates to about 3% of total error at 500 eV_{ee}.

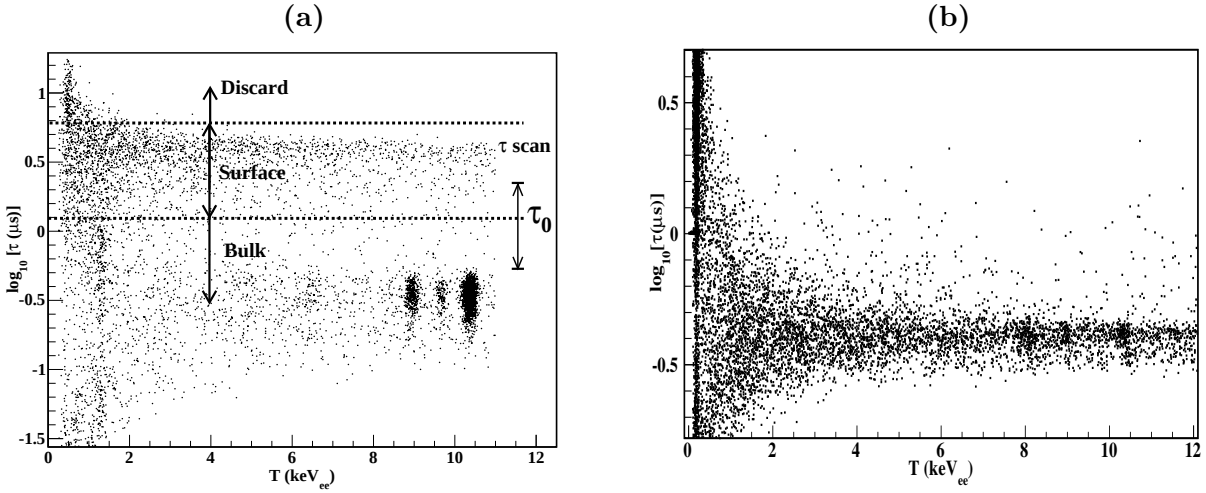

Figure 7. (a) pPCGe τ-distribution at low background configuration. τ_0 defines the surface-bulk selection criteria. (b) nPCGe τ-distribution at low background configuration and demonstrates the absence of anomalous surface events.

The width of the measured B and S band at $T < 1.5$ keV_{ee} is comparable to band separation and leads to merging of bands. Therefore, there exists contamination in B and S events. The evaluation of leakage factors and process to correct the measured spectra are further discussed in the section 3.1.

3.1. BS cut efficiencies measurement and correction

The calibration of BS cut requires measurement of bulk signal retaining ($\epsilon_{\rm BS}$) and surface background suppressing ($\lambda_{\rm BS}$) efficiencies. These efficiencies can be obtained by relating the observed rates (B,S) and actual rates (B_0,S_0) [15].

At lower energy, (B,S) and (B_0,S_0) are related by the following coupled equations:

$$\begin{aligned} \mathrm{B} &= \epsilon_{\rm BS} \cdot \mathrm{B}_0 \ + \ (1-\lambda_{\rm BS}) \cdot \mathrm{S}_0 \\ \mathrm{S} &= (1-\epsilon_{\rm BS}) \cdot \mathrm{B}_0 \ + \ \lambda_{\rm BS} \cdot \mathrm{S}_0 \ , \end{aligned} \tag{2}$$

with an additional unitarity constrain: B_0+S_0=B+S. The normalization assignment (B_0,S_0)=(B,S) is made on events within T_0=2.7-3.7 keV_{ee}. It is equivalent to setting $\epsilon_{\rm BS}$ and $\lambda_{\rm BS}$ to 1.0. This energy range is selected because it is above the complications of L-shell X-rays at ∼1 keV_{ee} as well as the physics region in dark matter analysis.

The derivation of ($\epsilon_{\rm BS}$,$\lambda_{\rm BS}$) therefore requires at least two measurements of (B,S) where the actual rates (B_0,S_0) are known. The data with ^{241}Am, ^{137}Cs and *in situ* cosmic-ray induced fast neutrons are used for obtaining $\epsilon_{\rm BS}$ and $\lambda_{\rm BS}$.

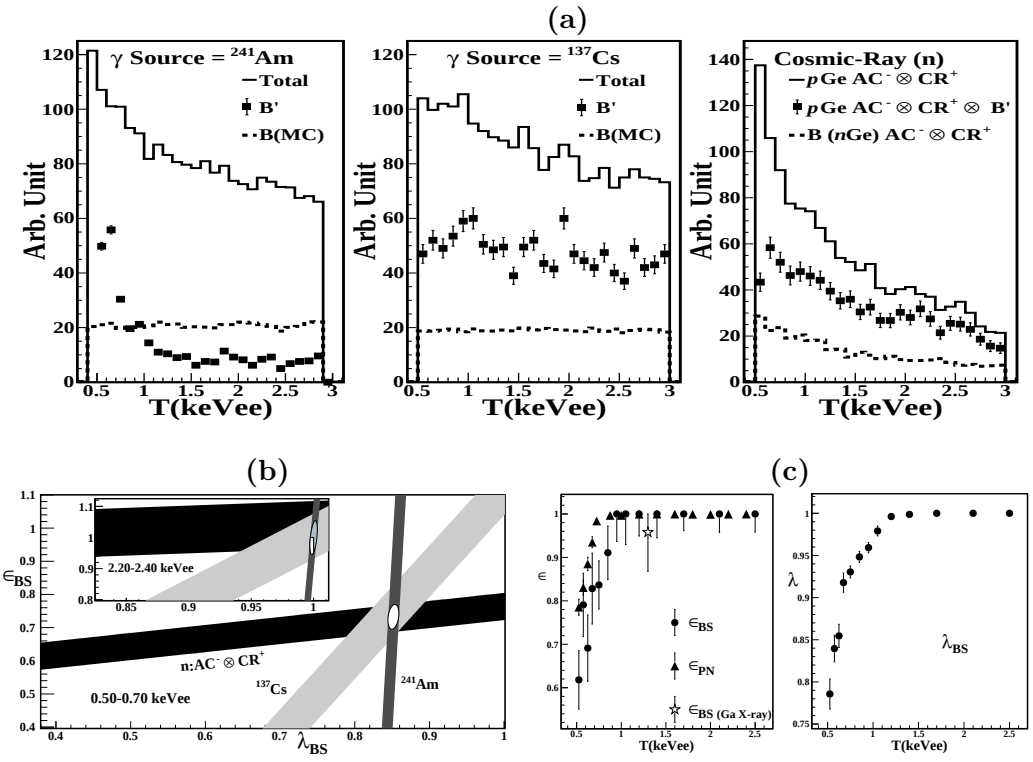

Figure 8. The derivation of $(\epsilon_{\rm BS}, \lambda_{\rm BS})$. (a) The measured Total and B′ spectra from pPCGE with surface-rich γ-ray (^{241}Am, ^{137}Cs) and bulk-rich cosmic-ray induced neutrons. They are compared to reference B-spectra acquired via simulations for γ-rays and nPCGe measurement for cosmic-neutrons. (b) Allowed bands at threshold and at a high energy band. (c) The measured ($\epsilon_{\rm BS}$,$\lambda_{\rm BS}$) and ϵ_{PN} as functions of energy. Independent measurement on $\epsilon_{\rm BS}$ with Ga-L X-rays is included.

The three chosen sources play a complementary role and these data samples are displayed in Figure 8a.
(I): Surface-rich γ-ray sources events− Calibrations with both low and high energy γ-sources (^{241}Am at 60 keVee and ^{137}Cs at 662 keVee, respectively) were performed. As displayed in Figure 8a, the measured B′-spectra are compared to the reference B derived from full simulation with surface layer thickness of 1.16 mm as input. The simulated B-spectra due to external γ-sources over a large range of energy are flat for T<10 keVee.
(II): Bulk-rich cosmic-ray induced fast neutrons events − A 523 g first-of-its-kind nPCGe detector was constructed. The components and dimensions are identical to pPCGe. The surface of nPCGe is a p^+ boron implanted electrode of sub-micron thickness. There are no anomalous surface effects. Data were taken under identical shielding configuration. The trigger efficiency was 100% above T=500 eVee, and energy calibration was obtained from standard internal X-ray lines. The AC$^-\otimes$ CR$^+$ condition selects cosmic-ray induced fast neutron events without associated γ-activities, which manifest mostly (∼85%) as bulk events. Accordingly, AC$^-\otimes$ CR$^+$ spectrum in nPCGe is taken as B-reference and compared with AC$^-\otimes$ CR$^+$ in pPCGe.

Using calibration data (I) and (II), ($\epsilon_{\rm BS}$,$\lambda_{\rm BS}$) are measured by solving the coupled Equation 2. Standard error propagation formulae are adopted to derive their uncertainties using errors in (B,B′,S′) as input. As examples, three allowed bands at threshold and at a high energy band are illustrated in Figure 8b. The different orientations of bands are consequences of different depth distributions of the samples, which give rise to different B:S ratios. The bands have common overlap regions, indicating the results are insensitive to event locations. The surface-rich γ-events and bulk-rich cosmic-ray induced neutron-events play complementary roles in constraining $\lambda_{\rm BS}$ and $\epsilon_{\rm BS}$, respectively. The results are depicted in Figure 8c, with ϵ_{PN} overlaid. By comparing the measured *in situ* Ga-L X-ray peak at 1.3 keVee after BS-selection to that predicted by corresponding K-peak at 10.37 keVee, a consistent $\epsilon_{\rm BS}$ is independently measured.

The efficiency-corrected ($\rm B_0$,$\rm S_0$) of physics samples can then be derived with the help of measured ($\epsilon_{\rm BS}, \lambda_{\rm BS}$) by the solution of Equation 2, and is given by

$$\begin{aligned} \rm B_0 &= \frac{\lambda_{BS}\cdot B-(1-\lambda_{BS})\cdot S}{(\epsilon_{BS}+\lambda_{BS}-1)} \\ \rm S_0 &= \frac{\epsilon_{BS}\cdot S-(1-\epsilon_{BS})\cdot B}{(\epsilon_{BS}+\lambda_{BS}-1)} \quad . \end{aligned} \tag{3}$$

The formulae can be understood as: $\rm B_0(S_0)$ should account for loss of efficiency in the measurement of B(S) in the first positive term, followed by a subtraction of leakage effect from S(B) in second negative term.

3.2. Error sources and assignment

The errors on ($\epsilon_{\rm BS}$,$\lambda_{\rm BS}$) are shown in Figure 8c. They are derived from global fits on allowed bands in Figure 8b. Standard error propagation techniques were applied to derive the resulting uncertainties on ($\rm B_0$,$\rm S_0$) via Equation 3. It can be noted from the Table 2 that the dominant error contribution is due to the statistical uncertainties of the physics data (as observations are associated with low count rate) and is boosted by $\frac{1}{(\epsilon_{\rm BS}+\lambda_{\rm BS}-1)}$.

Table 2. The contribution of uncertainties on $\rm AC^-\otimes CR^-\otimes B_0$ spectrum. † Errors are combined in quadrature and total error is normalized to 1.0.

Energy Bin	0.50−0.55 $\rm keV_{ee}$	1.90−1.95 $\rm keV_{ee}$
Measurement and Total Error ($\rm kg^{-1}keV^{-1}day^{-1}$)	10.6±5.0	6.1±1.6
Relative Contributions to Total Error† :		
I) Uncertainties on Calibration ($\epsilon_{\rm BS}$,$\lambda_{\rm BS}$) from Figure 8c :	0.26	<0.03
II) Measurement Error on $\rm B_0$ from Eq. 3 :		
Statistical Errors of (B,S)	0.41	0.99
Scaling by $1/(\epsilon_{\rm BS}+\lambda_{\rm BS}-1)$	2.29	1.00
Combined	0.95	0.99
III) Systematic Uncertainties due to Parameter Choice :		
(i) Rise-time Cut-Value τ_0	0.12	0.09
(ii) Fiducial Mass from Choice of τ_0	0.03	0.06
(iii) Normalization Range	0.13	0.07
(iv) ($\rm B_0$,$\rm S_0$)=(B,S) at Normalization	0.08	0.03
(v) Choice of Discard Region	0.05	0.001
Combined Systematic Error	0.20	0.12

4. Results and discussion

4.1. Energy spectrum

The $AC^- \otimes CR^-$ tagged events from pPCGe data taken at KSNL at various stages of analysis are depicted in Figure 9a. The measured-B and corrected-B_0 spectra are almost identical at $T > 1.5$ keV$_{ee}$, this is a direct consequence of $\epsilon_{BS} = \lambda_{BS} = 1$. At low energy, efficiency-correcting and background-subtracting effects compensate each other in this data set. After subtracting flat background due to high energy γ-rays and known L-shell X-rays contributions predicted accurately by measured higher energy K-peaks, the residual spectrum is shown in inset of Figure 9b.

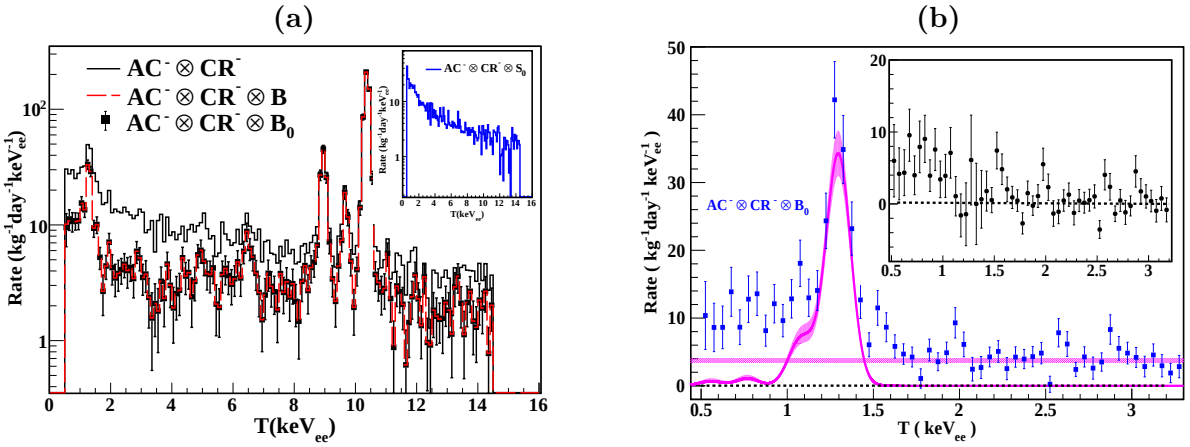

Figure 9. (a) Measured and corrected $AC^- \otimes CR^-$ tag spectra. (b) Shown in magenta are flat background due to high-energy γ-rays from ambient radioactivity, and contributions from the L-shell X-rays. The inset depicts the residual spectrum after background subtraction.

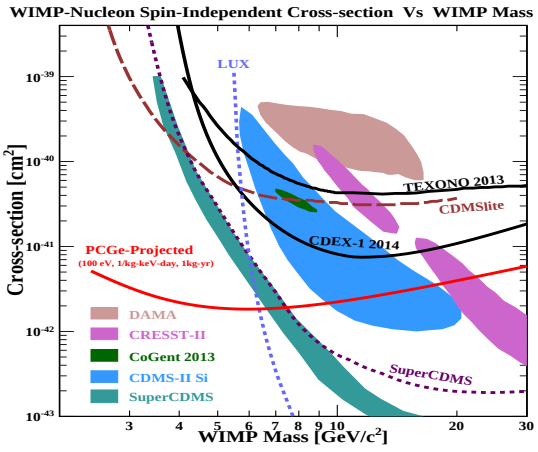

Figure 10. The 90% confidence level upper limit on $\sigma^{SI}_{\chi N}$ from TEXONO, CDEX-1 and other benchmark experiments.

4.2. Constrains on χN spin-independent interaction

The spectrum corresponding to χN candidate events is depicted in inset of Figure 9b. The Constraints on $\sigma^{SI}_{\chi N}$ were then derived via "binned Poisson" method with conventional astrophysical models[8] (local density of 0.3 GeV/cc and Maxwellian velocity distribution with v_0=220 km/s and v_{esc}=544 km/s). The event rates of χN spin-independent interaction cannot be larger than residual spectrum. The Ge quenching function is derived with TRIM software.

Exclusion plots for $\sigma^{\rm SI}_{\chi \rm N}$ versus m_χ at 90% confidence level from TEXONO [11] and CDEX-1 [14] are displayed in Figure 10, with other benchmark results superimposed [14]. The projected sensitivity at 100 eV_{ee} threshold, 1 kg-year data size and background at 1 cpkkd is also shown.

4.3. Constrains on electromagnetic properties of neutrino

The measurable spectra due to weak interactions, neutrino magnetic moments at $\mu_\nu = 10^{-11}\ \mu_{\rm B}$ and milli-charge ($|\delta_Q|$) at 10^{-12} for reactor neutrino flux of 10^{13} cm^{-2}s^{-1} are depicted in Figure 1. These are compared with various data set [3] and the corresponding limits at 90% CL are listed in Table 3. The limits on μ_ν and $|\delta_Q|$ from nPCGe data are $26.0 \times 10^{-11}\ \mu_{\rm B}$ and $2.1 \times 10^{-12}\ e_0$, respectively. $\mu_{\rm B}$ and e_0 are Bohr magneton and electron charge, respectively.

Table 3. A summary of experimental limits at 90% CL on neutrino electro-magnetic parameters using selected reactor neutrino data. The projected sensitivities of measurements at the specified realistically achievable experimental parameters are also shown.

Data Set	Reactor-$\bar{\nu}_e$ Flux ($\times 10^{13}$ cm^{-2}s^{-1})	Data Strength Reactor ON/OFF (kg-days)	Analysis Threshold (keV)	Bounds at 90% CL μ_ν ($10^{-11}\ \mu_{\rm B}$)	$\lvert\delta_Q\rvert$ ($10^{-12}\ e_0$)
CsI(Tl) - TEXONO [20]	0.64	29882.0/7369.0	3000	< 22.0	< 170
HPGe - GEMMA [21]	2.7	1133.4/280.4	2.8	< 2.9	< 1.1
nPCGe - TEXONO [6]	0.64	124.2/70.3	0.3	< 26.0	< 2.1
Projected [6]	2.7	800/200	0.1	< 1.7	< 0.06

References

[1] Giunti C and Studenikin A 2014 *arXiv:* **1403.6344** and references therein
[2] Wong H T and Li H B 2005 *Mod. Phys. Lett.* **A 20** 1103 and references therein
[3] Li H B 2003 *Phys. Rev. Lett* **90** 131802; Wong H T 2007 *Phys. Rev. D* 75 012001
[4] Davidson S, Gorbahn M and Santamaria A 2005 *Phys. Lett. B* **626** 151; Bell N F 2005 *Phys. Rev. Lett.* **95** 151802; Bell N F 2006 *Phys. Lett. B* **642** 377
[5] Kopeikin V I 1997 *Phys. Atom. Nucl.* **60** 2032; Fayans S A, Mikaelyan L A and Sinev V V 2001 *Phys. Atom. Nucl.* **64** 1475; Kouzakov K A, Studenikin A I and Voloshin M B 2011 *Phys. Rev.D* **83** 113001; Chen J W 2014 *Phys. Lett. B* **731** 159
[6] Chen J W 2014 *Phys. Rev. D* **90** 011301(R)
[7] Yue Q 2004 *HEP and Nucl. Phys.* **28** 877; Wong H T 2006 *J. Phys. Conf. Ser.* **39** 266; Wong H T 2011 *Int. J. Mod. Phys. D* **20** 1463
[8] Drees M and Gerbier G 2014 Chin. Phys. C**38** 353 and references therein
[9] Bertolini G and Coche A 1968 *Semiconductor detectors* Elsevier North Holland Amsterdam
[10] Wong H T 2008 *Mod. Phys. Lett. A* **23** 1431; Lin S T 2009 *Phys. Rev. D* **79** 061101(R)
[11] Li H B 2013 *Phys. Rev. Lett.* **110** 261301
[12] Soma A K 2014 *arXiv:* **1411.4802** [**physics.ins-det**] and references therein
[13] Liu S K 2014 *Phys. Rev. D* **90** 032003
[14] Kang K J 2013 *Chin. Phys. C* **37** 126002; Zhao W 2013 *Phys. Rev. D* **88** 052004; Yue Q 2014 *Phys. Rev. D* **90** 091701(R)
[15] Li H B 2014 *Astropart. Phys.* **56** 1
[16] Luke P N 1989 *IEEE Trans. Nucl. Sci. B* **36** 926
[17] Barbeau P S, Collar J I and Tench O 2007 *J. Cosmol. Astropart. Phys. B* **09** 009; Aalseth C E 2008 *Phys. Rev. Lett.* **101** 251301
[18] Aguayo E 2013 *Nucl. Instrum. Meth. A* **701** 176
[19] Press W H 2002 *Numerical Recipes in C* Second edition Cambridge University Press Chapter 14 Page 650
[20] Deniz M 2010 *Phys. Rev. D* **82** 033004; *arXiv[hep-ph]* **1006.1947**
[21] Beda A G 2012 *Adv. High Energy Phys.* **2012** 350150; Beda A G 2013 *Phys. Part. Nucl. Lett.* **10** 139